



Improved Mass and Radius Constraints for Quiescent Neutron Stars in Omega Cen and NGC 6397

Citation

Heinke, C. O., H. N. Cohn, P. M. Lugger, N. A. Webb, W. C. G. Ho, J. Anderson, S. Campana, et al. 2014. "Improved Mass and Radius Constraints for Quiescent Neutron Stars in Cen and NGC 6397." *Monthly Notices of the Royal Astronomical Society* 444 (1) (August 16): 443–456. doi:10.1093/mnras/stu1449.

Published Version

doi:10.1093/mnras/stu1449

Permanent link

<http://nrs.harvard.edu/urn-3:HUL.InstRepos:30168201>

Terms of Use

This article was downloaded from Harvard University's DASH repository, and is made available under the terms and conditions applicable to Open Access Policy Articles, as set forth at <http://nrs.harvard.edu/urn-3:HUL.InstRepos:dash.current.terms-of-use#OAP>

Share Your Story

The Harvard community has made this article openly available.
Please share how this access benefits you. [Submit a story](#).

[Accessibility](#)

Improved Mass and Radius Constraints for Quiescent Neutron Stars in ω Cen and NGC 6397

C. O. Heinke^{1*}, H. N. Cohn², P. M. Lugger², N. A. Webb³, W. C. G. Ho⁴,
J. Anderson⁵, S. Campana⁶, S. Bogdanov⁷, D. Haggard⁸, A. M. Cool⁹, J. E. Grindlay¹⁰

¹*Dept. of Physics, University of Alberta, CCIS 4-183, Edmonton, AB T6G 2E1, Canada*

²*Department of Astronomy, Indiana University, 727 E. Third St, Bloomington, IN 47405, USA*

³*Universite de Toulouse, UPS-OMP, IRAP, Toulouse, France; CNRS, IRAP, 9 Av. Colonel Roche, BP 44346, F-31028 Toulouse, Cedex 4, France*

⁴*Mathematical Sciences & STAG Research Centre, University of Southampton, Southampton SO17 1BJ, UK*

⁵*Space Telescope Science Institute, 3700 San Martin Drive, Baltimore, MD 21218, USA*

⁶*INAF - Osservatorio astronomico di Brera, Via Bianchi 46, Merate I-23807 (LC), Italy*

⁷*Columbia Astrophysics Laboratory, Columbia University, 550 West 120th Street, New York, NY 10027, USA*

⁸*CIERA, Physics and Astronomy Department, Northwestern University, 2145 Sheridan Road, Evanston, IL 60208, USA; CIERA Fellow*

⁹*Department of Physics and Astronomy, San Francisco State University, 1600 Holloway Avenue, San Francisco, CA 94132, USA*

¹⁰*Harvard-Smithsonian Center for Astrophysics, 60 Garden Street, Cambridge, MA 02138, USA*

6 June 2014

ABSTRACT

We use *Chandra* and *XMM-Newton* observations of the globular clusters ω Cen and NGC 6397 to measure the spectrum of their quiescent neutron stars (NSs), and thus to constrain the allowed ranges of mass and radius for each. We also use *Hubble Space Telescope* photometry of NGC 6397 to identify a potential optical companion to the quiescent NS, and find evidence that the companion lacks hydrogen. We carefully consider a number of systematic problems, and show that the choices of atmospheric composition, interstellar medium abundances, and cluster distances can have important effects on the inferred NS mass and radius. We find that for typical NS masses, the radii of both NSs are consistent with the 10 – 13 km range favored by recent nuclear physics experiments. This removes the evidence suggested by Guillot and collaborators for an unusually small NS radius, which relied upon the small inferred radius of the NGC 6397 NS.

Key words: Globular clusters – X-rays: binaries – stars: neutron – dense matter

1 INTRODUCTION

The behaviour of matter at extremely high densities cannot be measured in laboratories on Earth, but can be probed through measurements of the properties of neutron stars (NSs). Some NS properties can be measured accurately without systematic uncertainties, such as their rotation rates, velocities, and, for some, their gravitational masses. However, effective constraints on the interior makeup of NSs (and thus, their equation of state) require robust measurements of both mass and radius, ideally for several NSs (Lattimer & Prakash 2007). Recent attention has focused on thermal surface radiation from NSs, during thermonuclear bursts and/or during periods of quiescence (Özel, Baym & Güver 2010; Guillot et al. 2013). Both the apparent surface area and

the NS’s Eddington limit can be tested during observations of thermonuclear bursts, thus providing orthogonal constraints, but a number of systematic uncertainties (e.g. anisotropies, variations in the persistent emission, the radius of emission, the details of the spectrum) remain unresolved (e.g. Steiner, Lattimer & Brown 2010; Zambir, Cumming & Galloway 2012; Galloway & Lampe 2012; Worpel, Galloway & Price 2013).

Fewer systematic uncertainties surround measurements of the radiation radius of quiescent NSs, or quiescent low-mass X-ray binaries (qLMXBs) in globular clusters (Rutledge et al. 2002a). The distances to globular clusters are well-known, with a 6% rms variation among different distance measurement techniques (Woodley et al. 2012). NSs in qLMXBs produce thermal (blackbody-like) X-rays due to heating of the NS core (and crust) during periods of accretion (Brown, Bildsten & Rutledge 1998; Rutledge et al. 2002b),

* heinke@ualberta.ca

and seem to produce both thermal X-rays and nonthermal X-rays (typically fit with a power-law) by accretion, though other physics may be involved in the poorly-understood power-law (Campana et al. 1998; Cackett et al. 2010; Deufel, Dullemond & Spruit 2001). NSs in qLMXBs are believed to have low magnetic fields, and in most cases pure hydrogen atmospheres, allowing for robust physical modeling (Zavlin, Pavlov & Shibano 1996; Rajagopal & Romani 1996; Heinke et al. 2006; Haakonsen et al. 2012). The constraints in mass and radius from these measurements are degenerate along a curved track, close to a line of constant $R_\infty = R/\sqrt{1 - 2GM/(Rc^2)}$, where M and R are the NS mass and radius, and R_∞ is the radius as seen at infinity (e.g. Heinke et al. 2006). This is due to gravitational redshift increasing with increasing mass, shifting the intrinsic NS temperature to higher values, and thus requiring a smaller emitting surface area.

Numerous qLMXBs are known in globular clusters (e.g. Heinke et al. 2003; Guillot et al. 2009), of which a handful are sufficiently bright and well-observed to provide interesting constraints on mass and radius (e.g., in 47 Tuc, Heinke et al. 2006; in NGC 6397, Guillot, Rutledge & Brown 2011; in ω Cen and M13, Webb & Barret 2007; in M28, Servillat et al. 2012). However, radius measurements of NSs in globular cluster qLMXBs reveal significant discrepancies, with the inferred radii for some NSs appearing significantly larger or smaller than the inferred radii for other NSs (e.g. Webb & Barret 2007). We particularly note the Bayesian multi-object analysis of Guillot et al. (2013), who conducted a simultaneous spectral analysis of five qLMXBs in globular clusters to measure the NS radius. They prefer an extremely small radius for the qLMXB U24 in NGC 6397 ($R_\infty = 8.4^{+1.3}_{-1.1}$ km, or $R = 6.6^{+1.2}_{-1.1}$ km), and an extremely large radius or mass for the ω Cen qLMXB ($R_\infty = 23.6^{+7.6}_{-7.1}$ km, or $R = 20.1^{+7.4}_{-7.2}$ km). Although a single NS equation of state can pass through both of these mass-radius regions (at nearly constant radius in the relevant mass range), this would generally require unphysically low masses ($< 1 M_\odot$) for U24, and rather large masses ($> 2 M_\odot$) for the ω Cen NS.

This work is motivated by a desire to see if these NS measurements can be reconciled. We are also interested in investigating the effect of systematic uncertainties in the chemical composition of the NS atmosphere and in the modeling of the interstellar medium. We utilize our new deep *Chandra* observations of ω Cen, along with archival *Chandra* observations of NGC 6397. We also use results from our deep *Hubble Space Telescope* (*HST*) observations of NGC 6397 to constrain the nature of the companion to U24 in NGC 6397. Before describing the data and our analysis, we discuss some systematic problems we consider here (not an exhaustive list; see e.g. Guillot, Rutledge & Brown 2011, AlGendy & Morsink 2014, and finally Elshamouty et al. in prep., for limits on, and detailed consideration of the effects of, temperature inhomogeneities).

1.1 Systematics: Atmosphere Composition

Ionized hydrogen atmospheres (for low magnetic fields and temperatures relevant to our problem, $> 3 \times 10^5$ K, Zavlin, Pavlov & Shibano 1996, the atmosphere is

completely ionized) alter the outgoing flux from the surface through free-free absorption. The opacity dependence of this absorption is roughly ν^{-3} , meaning that the observed flux is shifted to higher energies, while appearing roughly blackbody in shape (Romani 1987; Zavlin, Pavlov & Shibano 1996; Rajagopal & Romani 1996). The timescale of only a few seconds for elements to stratify in a NS atmosphere, means that the lowest-density element will rise to the surface (Alcock & Illarionov 1980; Hameury, Heyvaerts & Bonazzola 1983; Brown, Bildsten & Chang 2002), unless heavier elements are being deposited at a high rate, translating to an accretion luminosity of roughly 10^{33} ergs/s (Rutledge et al. 2002a). Such an accretion rate may be experienced by, e.g., Aquila X-1 in some quiescent observations, based on its variability properties. Aquila X-1 may also show evidence of features in its spectrum from heavier elements (Rutledge et al. 2002a). If the accreted material possesses hydrogen, and the luminosity is well below 10^{33} ergs/s (or shows a total lack of evidence of accretion, Heinke et al. 2006) the emitted spectrum of the NS should be well-represented by a hydrogen atmosphere model. The hydrogen atmosphere models constructed by different groups give reproducible results (Zavlin, Pavlov & Shibano 1996; Lloyd 2003; Heinke et al. 2006; Haakonsen et al. 2012), indicating that parameters derived from hydrogen atmosphere modeling should be accurate to within a few percent (Haakonsen et al. 2012).

However, the accreted material may not possess any hydrogen, if the donor star is a white dwarf. It is possible that the accreted material may spallate on impact, producing protons (Bildsten, Salpeter & Wasserman 1993), but spallation may require infalling protons that would not be present if the donor star is a white dwarf (in't Zand et al. 2005). Also, the creation of hydrogen would alter the character of observed thermonuclear bursts from NSs accreting from white dwarfs, which show distinct properties consistent with the absence of hydrogen (e.g. Cumming 2003). White dwarf donors have been confirmed (by orbital period measurement) for five luminous (persistent or transient, reaching $L_X > 10^{35}$ ergs/s) NS X-ray binaries in globular clusters, out of 18 such sources (of which 10 are confirmed not to have white dwarf donors; Zurek et al. 2009; Altamirano et al. 2010; Bahramian et al. 2013).

Thus, there is good reason to expect the presence of qLMXBs in globular clusters with helium (or possibly carbon) atmospheres. Helium atmospheres generally resemble hydrogen atmospheres (Romani 1987), but are slightly harder—the difference between the color temperature and the effective surface temperature is slightly larger than for hydrogen atmospheres (Ho & Heinke 2009). Helium atmosphere models will thus predict different best-fit values of mass and radius for observed spectra. (Carbon atmospheres are significantly harder, and show a strong edge near 0.3 keV; Ho & Heinke 2009. We do not consider carbon atmospheres further in this work, as they seem inapplicable to the qLMXBs of interest; fitting a carbon atmosphere would give much larger inferred radii.) We have applied the helium models of Ho & Heinke (2009) to the high-quality X-ray spectra of qLMXBs in M28 (Servillat et al. 2012) and M13 (Catuneanu et al. 2013), finding significantly larger inferred values of R_∞ (and thus, larger masses or radii) for

helium than hydrogen models. This motivates us to consider fitting a helium atmosphere model to U24 in NGC 6397, as its inferred radius, for a hydrogen atmosphere, is rather small (Guillot et al. 2013; Lattimer & Steiner 2014). Note that the donor to the qLMXB in ω Cen is known to possess hydrogen, through detection of H α in emission (Haggard et al. 2004).

1.2 Systematics: Interstellar Medium

Extinction by the interstellar medium (ISM) significantly affects the inferred radius of the NSs (Lattimer & Steiner 2014). Thus, careful modeling of the ISM is critical. The absorption of X-rays is principally due not to hydrogen, but to the heavier elements in the ISM, so their relative abundances will affect the shape of the absorbed flux. Current modeling of the abundances and cross-sections of the ISM (Wilms, Allen & McCray 2000, incorporated as the **tbabs** model in XSPEC) show significant differences with older models such as Morrison & McCammon (1983), incorporated as the **wabs** model used by Guillot et al. (2013). We will test whether the choice of absorbing model makes a difference here.

Lattimer & Steiner (2014) raise the question of whether the interstellar absorption column, N_H , for each qLMXB in a globular cluster should be fixed to the value derived from an independent HI survey (such as Dickey & Lockman 1990) in the direction of the cluster, arguing that fixing N_H in this manner gives more consistent R_∞ values for different NSs, and that the locus of R_∞ measurements is more consistent with predictions of the equation of state from nuclear experiments and theoretical neutron matter studies. Fixing N_H to values from an HI survey has clear flaws, since the HI surveys account only for atomic H, include all H along the line of sight (some of which may lie behind the cluster), and are integrated over large angular scales (possibly not representative of the particular line of sight). Optical measurements of the extinction towards the globular cluster are superior to HI surveys (as they avoid these problems), but may suffer from uncertainty in the transformation from A_V to N_H (based, e.g., on uncertain abundances), and do not allow for the possibility of extra N_H intrinsic to the binary system. Spectral fitting of X-ray data gives a direct measurement of the N_H experienced along the line of sight, and should be used if accurate constraints on NS radii are desired. For our analyses in this paper, we measure the N_H directly from the qLMXB X-ray spectra without any external constraints. We find that these measurements are typically close to the N_H values calculated from the measured A_V to each cluster (and are often closer to these values than to the N_H inferred from independent HI surveys), but that in some cases they are significantly different.

1.3 Systematics: Distance to Globular Clusters

The distances to globular clusters are a topic of great importance for stellar evolution and cosmology studies (Krauss & Chaboyer 2003). No method of measuring distances to globular clusters is completely without systematic uncertainties. Guillot et al. (2013) prefer dynamical methods (comparing radial velocities to proper motions) for measuring distances, using the argument that the uncertainties

in these methods are well-understood. However, this understates the systematic uncertainties in dynamical distance derivations, coming from the use of different stars for the radial velocities and the proper motions, and from the assumption of isotropy in velocities.

For ω Cen, the dynamical distance estimate by van de Ven et al. (2006) is based on thorough dynamical modeling of an inclined, axisymmetric, rotating ellipsoid, giving a distance of 4.8 ± 0.3 (1σ) kpc. This measurement may be slightly underestimated if some interloping stars remain in the proper motion data, and particularly by the systematic offset between the proper motions of the metal-rich RGB stars and the metal-poor RGB and HB populations (Platais et al. 2003; van de Ven et al. 2006). Distance determinations using modeling of eclipsing binaries (5.36 ± 0.3 kpc, Thompson et al. 2001), RR Lyrae near-IR photometry (5.5 ± 0.04 kpc, Del Principe et al. 2006), and the edge of the RR Lyrae instability strip (5.6 ± 0.3 kpc, Caputo, degl’Innocenti & Marconi 2002) are larger, while SED modeling of giants gives 4.85 ± 0.2 kpc (McDonald et al. 2009). The homogeneously calculated horizontal-branch distances of Harris (1996) (2010 revision)¹ give an ω Cen distance of 5.2 kpc. Bono et al. (2008) measure the distance ratio between ω Cen and the better-studied cluster 47 Tuc with three different relative methods, all indicating that ω Cen is 16% ($\pm 3\%$) farther than 47 Tuc. Woodley et al. (2012) average 22 published distance measurements for 47 Tuc to find $d_{47Tuc} = 4.57$ kpc (standard deviation of 0.28 kpc, error in mean of 0.06 kpc), in agreement with the best white dwarf distance measurement to 47 Tuc by Hansen et al. (2013) of 4.61 ± 0.19 kpc. Using this average distance for 47 Tuc, with its error in the mean, with the relative distance determination above, implies that $d_{\omega Cen} = 5.30 \pm 0.17$ kpc. We choose for this paper to adopt 5.30 ± 0.17 kpc as our standard for ω Cen’s distance.

NGC 6397 has been the subject of recent high-quality distance measurements using the white dwarf cooling sequence (Hansen et al. 2007, 2.54 ± 0.07 kpc; Strickler et al. 2009, 2.39 ± 0.13 kpc using Hansen’s WD mass estimate), and main-sequence fitting (Gratton et al. 2003, 2.52 ± 0.10 kpc). The Harris (1996) (2010 revision) catalog calculates a horizontal branch distance of 2.3 kpc for NGC 6397. Guillot et al. (2013) use a dynamical distance measurement of 2.02 ± 0.18 kpc obtained by Rees (1996).² Heyl et al. (2012) performed a higher-quality dynamical distance measurement, using multiple deep *HST* observations to obtain proper motions, obtaining a final measurement of $2.2^{+0.5}_{-0.7}$ kpc with minimal systematic errors, or a more precise measurement of 2.0 ± 0.2 kpc that is more vulnerable to systematic uncertainties (as the same stars are not used for radial velocities vs. proper motions). Dynamical distance methods generally assume no anisotropies among the stellar velocities, which could bias the calculated distance; such anisotropies have been measured by Richer et al. (2013) in 47 Tuc. A relative distance comparison of NGC 6397 to 47

¹ <http://physwww.physics.mcmaster.ca/~harris/mwgc.dat>

² The dynamical distance measurement of Rees (1996) is not explained in detail, is not peer-reviewed (it is only listed in a conference proceeding), and is referred to as “preliminary” in a later conference proceeding by the same author Rees (1997).

Tuc (Hansen et al. 2013) finds that NGC 6397 is 1.32 ± 0.10 magnitudes closer, or $54.5 \pm 2.5\%$ of 47 Tuc’s distance. Using the Woodley et al. 47 Tuc average distance measurement, we thus derive a distance of 2.51 ± 0.07 kpc. Therefore, we choose a standard distance of 2.51 ± 0.07 kpc, which aligns with the most accurate relative distance measurements, and is consistent (via relative distance measurements of each cluster to 47 Tuc) with our choice for ω Cen above.

1.4 Systematics: Instrumental Calibration

The absolute calibration of X-ray instruments, and particularly the cross-calibration between the *XMM-Newton* pn and MOS, and *Chandra* ACIS, detectors, is a topic of active research by the International Astronomical Consortium for High Energy Calibration (IACHEC) calibration consortium³. However, it has rarely been discussed in the literature on qLMXB radius measurements, with the exception of Catuneanu et al. (2013). Both the normalization of the X-ray flux, and the spectral shape measurements, show differences between different detectors. Tsujimoto et al. (2011), comparing *Chandra*/ACIS, *XMM-Newton* pn and MOS, *Suzaku*/XIS and *Swift*/XRT spectra of the absorbed pulsar wind nebula G21.5-0.9 (1–8 keV), found that the *Chandra*/ACIS detector measured fluxes 10% higher than the average, while the *XMM-Newton*/pn detector measured fluxes 10% lower than the average among other detectors. Nevalainen, David & Guainazzi (2010), comparing *Chandra*/ACIS and *XMM-Newton*/EPIC observations of galaxy clusters, found that the 2–7 keV EPIC and ACIS fluxes were only 5–10% different. However, measurement of cluster temperatures in the 0.5–2 keV band gave differences of 18% between the *Chandra*/ACIS and *XMM-Newton*/pn, due to the ratio of ACIS data to the best pn model fit declining from 1.0 at 2 keV, to 0.9 at 0.5 keV. Since qLMXB thermal spectra provide most of their counts between 0.5 and 2 keV, this suggests that *Chandra*/ACIS and *XMM-Newton*/pn will give diverging results at very high S/N ratios. We will investigate this question below for the ω Cen spectra, by including fits allowing the temperature, or a normalization constant between detectors, to vary.

2 OBSERVATIONS

2.1 ω Cen: *Chandra*, *XMM-Newton* Data

The available X-ray data on the ω Cen qLMXB (summarized in Table 1) include a 2001 *XMM-Newton* EPIC observation (Gendre, Barret & Webb 2003), two 2000 ACIS-I *Chandra* observations totaling 69 ks (Haggard, Cool & Davies 2009), and two deeper 2012 ACIS-I *Chandra* observations totaling 222 ks (Haggard et al. 2013).

XMM-Newton observation 112220101 lasted 40 ks, collecting usable exposures on the quiescent NS of 33.5 ks with the pn, and 39.5 ks with the MOS1 and MOS2 detectors, all in full-frame mode with the medium filter. We reduced the

data using SAS 13.0,⁴ running `emchain` and `epchain` and filtering the event lists to retain predefined patterns 0–12 and use the `#XMMEA_EM` screening flags for MOS data, and retain patterns 0–4 and use the `#XMMEA_EP` flags for pn data. We used an extraction region of 19” (as determined by Guillot et al. 2013 to maximize the signal-to-noise ratio), and extracted background from a nearby region on the same chip. The background was low and fairly stable for the entire observation, so we used the entire valid exposure time.

We reprocessed the *Chandra* observations using CIAO v.4.5 (Fruscione et al. 2006), correcting the data for charge transfer efficiency, and without using very-faint mode cleaning to reduce the background (as this can remove real data from sources of moderate brightness). We extracted spectra from a 4” radius extraction region (to deal with the relatively large point-spread function at the 4.4’ off-axis angle), and a nearby, larger background region, using the `specextract` CIAO script. This includes the `arfcorr` task that applies an energy-dependent correction of the effective area for the fraction of the point-spread function extracted.

We combined the *Chandra* spectra taken at the same epochs, combined the two MOS spectra, and grouped each spectrum to at least 20 counts/bin to permit the use of χ^2 statistics. No energy bin has a majority of counts outside the calibrated *Chandra* energy range (0.277–9.886 keV). We ignored spectral bins below 0.2 keV for *XMM-Newton* data.

2.2 NGC 6397: *Chandra* Data

There are five available *Chandra* observations of NGC 6397 (Table 1); one 48 ks ACIS-I observation taken in 2000 (Grindlay et al. 2001), and pairs of ACIS-S observations in 2002 (totaling 55 ks) and in 2007 (totalling 237 ks; Bogdanov et al. 2010). All of these observations were analyzed by Guillot, Rutledge & Brown (2011). We reprocessed the *Chandra* observations using CIAO v.4.5, correcting the data for charge transfer efficiency, and without using the very-faint mode cleaning to remove background. We extracted spectra from a 2.5” radius extraction region, and a nearby, larger background region, using the `specextract` CIAO script, including energy-dependent correction of the effective area for the fraction of the point-spread function extracted. We grouped each spectrum to at least 20 counts/bin, except ObsID 7460 of NGC 6397 (the highest-quality spectrum, with 3124 counts) which we binned to at least 40 counts/bin. We verified that different choices of binning do not significantly alter the results presented here.

2.3 NGC 6397: HST Data

Our dataset is described in Strickler et al. (2009) and Cohn et al. (2010); we provide a concise synopsis here (summarized in Table 1). We used the *HST* GO-10257 data set (PI: Anderson), consisting of deep, highly dithered ACS/WFC images targeting the center of NGC 6397 in

³ <http://web.mit.edu/iachec/papers/index.html>

⁴ The *XMM-Newton* SAS is developed and maintained by the Science Operations Centre at the European Space Astronomy Centre and the Survey Science Centre at the University of Leicester.

Table 1. *Chandra* and *HST* data used

Telescope	Instr./filter	ID	Date	Exp. time
ω Cen				
<i>Chandra</i>	ACIS-I	653	2000 Jan. 24	25 ks
<i>Chandra</i>	ACIS-I	1519	2000 Jan. 25	44 ks
<i>Chandra</i>	ACIS-I	13727	2012 Apr. 16	49 ks
<i>Chandra</i>	ACIS-I	13726	2012 Apr. 17	174 ks
<i>XMM-Newton</i>	EPIC/medium	112220101	2001 Aug. 12	40 ks
NGC 6397				
<i>Chandra</i>	ACIS-I	79	2000 Jul. 31	48 ks
<i>Chandra</i>	ACIS-S	2668	2002 May 13	28 ks
<i>Chandra</i>	ACIS-S	2669	2002 May 15	27 ks
<i>Chandra</i>	ACIS-S	7461	2007 Jun. 22	89 ks
<i>Chandra</i>	ACIS-S	7460	2007 Jul. 16	148 ks
<i>HST</i>	ACS/WFC/F435W	10257	2004 Aug–2005 Jun	1765 s
<i>HST</i>	ACS/WFC/F625W	10257	2004 Jul–2005 Jun	1750 s
<i>HST</i>	ACS/WFC/F658N	10257	2004 Jul–2005 Jun	15700 s

F435W (B), F625W (R), and F658N ($H\alpha$), over 10 single-orbit epochs, roughly once per month between 2004 July and 2005 June. The data include 5 short B (13 s), 5 long B (340 s), 5 short R (10 s), 5 long R (340 s), and 40 $H\alpha$ (390 s or 395 s) exposures, where the short exposures fill in photometry for stars that saturate in the long exposures. The large number of $H\alpha$ frames produces a stacked $H\alpha$ image with exceptionally good PSF sampling.

3 NGC 6397: HST ANALYSIS

Cohn et al. (2010) report an analysis of the *HST* dataset described above, searching for optical counterparts for *Chandra* X-ray sources. The star finding and photometry for this analysis used the software described in Anderson et al. (2008), developed for the ACS Globular Cluster Treasury project. Briefly, this software searches for pixels that are higher than their eight neighbours (local peaks) in each separate exposure, and identifies real stars at locations which are peaks in more than a specified threshold fraction of the exposures. It then measures the brightness of each star in each exposure, both individually and simultaneously, using a spatially variable library of PSFs. This analysis did not detect any star within the error circle of U24, the qLMXB in NGC 6397, although there are two relatively bright stars only $\sim 0.6''$ away from the center of the error circle, which has radius $0.285''$ (at 95% confidence; Bogdanov et al. 2010). However, Cohn et al. (2010) did note a “hint of detection in R only” for U24 in their Table 1 owing to the presence of “a small ‘blip’ near the center of the error circle in the stacked R image.” They suggested that it “likely represents the combination of Airy ring artifacts” from the two nearby bright stars.

We have conducted new photometry directly on the stacked images of this *HST* dataset, in order to assess the possibility that the detection of a U24 counterpart in R is real. We utilized two different methods for the stacking, the STSDAS *astrodrizzle* software (based on the drizzle algorithm, Fruchter & Hook 2002), and stacking using the

method described in Anderson et al. (2008). Both methods involve oversampling the images by a factor of two. The stacked images (using *astrodrizzle*) are presented in Figure 1. Inspection reveals evidence for a faint star at the center of the error circle in the R image; this was evident with either stacking approach. Although the possible object is in a noisy region of the image due to the wings of the PSF from the two much brighter stars, the image suggests that this is a real, albeit weak, detection. By careful aperture photometry, we estimate an R magnitude of 26.2 ± 0.3 for this star (setting our zeropoints to those of Strickler et al. 2009 and estimating the uncertainty from the systematic error in determining the sky background). At NGC 6397’s distance and extinction, this corresponds to $M_R = 13.7$, which corresponds to a maximum mass for the companion star (if a main-sequence star) of $\lesssim 0.089 M_\odot$ (Baraffe et al. 1997), and maximum $T_{\text{eff}} = 2900$ K.

We do not find evidence for a faint star at the location of the R -band candidate counterpart to U24 in the B or $H\alpha$ images (see Fig. 1). In order to place an upper limit on the possible flux enhancements in these bands, artificial stars with a range of magnitudes were placed at this position. The faintest magnitude that produced a discernible flux enhancement was taken as representing the upper flux limit. This resulted in limits in $B > 26.8$ and $H\alpha > 25.5$. Thus, we find that $B - R > 0.6$ and $H\alpha - R > -0.7$. We have plotted these photometric limits on the CMDs reported by Cohn et al. (2010) in Fig. 2. Examination of these CMDs indicates that the possible counterpart to U24 is consistent with being no bluer than about the white dwarf sequence colour at this magnitude and with showing no evidence for an $H\alpha$ excess relative to the main sequence.

The main sequence is difficult to identify at these magnitudes. However, comparison with the ultra-deep *HST* imaging of NGC 6397 by Richer et al. (2008) shows that the disappearance of the clear main sequence at $R \sim 25$ is largely due to the main sequence luminosity function dropping off, as luminosity falls off dramatically with decreasing mass close to the hydrogen-burning limit. The lack of a well-defined main sequence forces us to calculate the

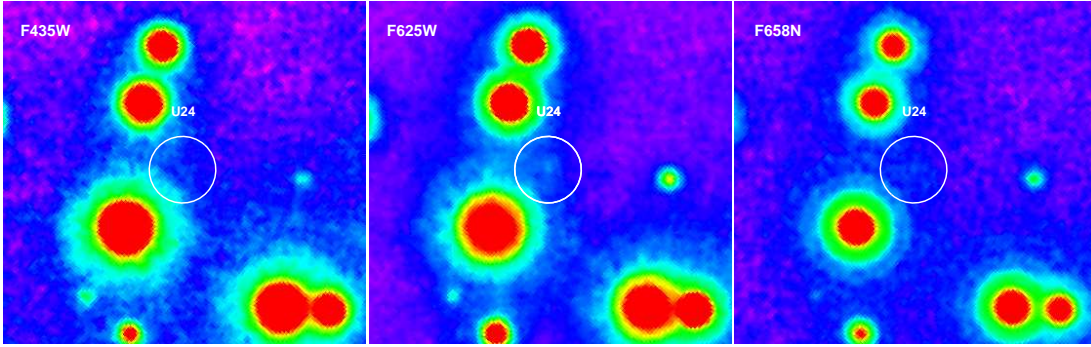


Figure 1. Combined, oversampled, *astrodrizzled* *HST* ACS/WFC images of the region surrounding U24 in NGC 6397. Left: combined *B* image. Middle: combined *R* image. Right: combined $H\alpha$ image. A possible star, and potential counterpart to U24, may be identified at the center of the $0.285''$ error circle in the *R* image, but is not present in the other frames.

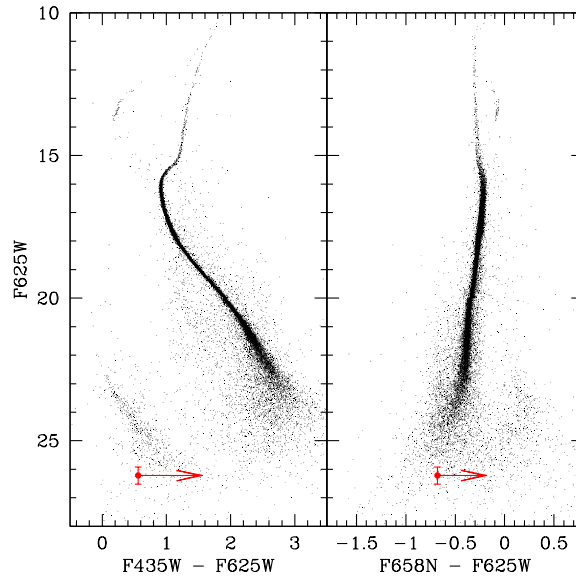


Figure 2. Left: *HST* ACS/WFC color-magnitude diagram of NGC 6397 in the *B* and *R* filters. The possible U24 counterpart is represented by an error bar with a horizontal arrow indicating the limit on its *B*–*R* color based on its nondetection in *B*. Right: *HST* ACS/WFC color-magnitude diagram of NGC 6397 in the $H\alpha$ and *R* filters. The possible U24 counterpart is again represented by an error bar with a horizontal arrow indicating the limit on its $H\alpha$ excess based on its nondetection in $H\alpha$.

$H\alpha$ –*R* colour of main-sequence stars at this position. We use SYNPHOT to compute the $H\alpha$ –*R* colour of a Pickles M5V 2950 K stellar model, using the appropriate extinction and ACS filters, finding $H\alpha$ –*R*=−0.75, which is consistent with the general trend of the main sequence at brighter magnitudes. We can thus estimate the $H\alpha$ excess relative to the main sequence, $\Delta H\alpha$, should not be larger than −0.25 mags (accounting for the uncertainty on our *R* magnitude). We can then estimate a limit on the equivalent width (EW) of $H\alpha$ in U24, using $EW(H\alpha)=RW \times [1-10^{-0.4 \times \Delta H\alpha}]$ (De Marchi, Panagia & Romaniello 2010), where *RW* is the rectangular width of the ACS/WFC $H\alpha$ filter in Å, i.e. 75 Å. This gives us an upper limit of 19 Å on the EW of $H\alpha$ for the putative U24 counterpart.

We can use this information to consider the possible nature of U24. Quiescent LMXBs generally show strong $H\alpha$

emission, much stronger than during outbursts (when the optical emission is dominated by reprocessing of X-rays). Fender et al. (2009) show that typical EWs for $H\alpha$ of black hole LMXBs in quiescence are 30–300 Å, but they have only three literature datapoints for NS LMXBs in quiescence, so we increase their sample here. Shahbaz et al. (1996) found Cen X-4 to show an $H\alpha$ EW of 48 Å, Torres et al. (2002) an EW of 35 ± 7 Å, and D’Avanzo et al. (2005) an EW of 40 Å. Garcia et al. (1999) found 9.5 Å for Aql X-1 in quiescence, while Shahbaz et al. (1996) found 4 Å, but all quiescent spectra of Aql X-1 before 1999 refer to the combined spectrum of Aql X-1 with its brighter, eastern neighbour $0.48''$ away (Chevalier et al. 1999). The companion-subtracted quiescent spectrum of Aquila X-1 shown in Chevalier et al. (1999) suggests an EW of 30–40 Å. Casares et al. (2002) show that XTE J2123-058 shows an EW of 20 Å in $H\alpha$ in quies-

cence. Campana et al. (2004) find a 10 Å EW for SAX J1808.4-3658, but this spectrum combines SAX J1808.4-3658 with a neighbour of similar brightness 0.5" away (Hartman et al. 2008; Deloye et al. 2008), so we may estimate (taking the continuum flux to be halved) a $\gtrsim 20$ Å EW for SAX J1808.4-3658. Bassa et al. (2009) measure a 31 Å H α EW for EXO 0748-676 in quiescence. The qLMXB in ω Cen exhibited a ~ 1 magnitude H α excess (Haggard et al. 2004), giving an estimated ~ 110 Å EW. Beccari et al. (2014) use H α , V and I photometry to calculate H α EWs of 28 Å and 50 Å for the quiescent NS LMXBs W125 and W58/X5 in the globular cluster 47 Tuc. Finally, three systems (PSR J1023+0038, M28I=IGR J18245-2452, and XSS J12270-4859) swing between radio pulsations and active accretion (Archibald et al. 2009; Papitto et al. 2013; Bassa et al. 2014). These three systems show no evidence of H α emission (or other disc signatures) when in their radio pulsar state (Thorstensen & Armstrong 2005; Pallanca et al. 2013; Bassa et al. 2014), but show H α EWs of 14-19 Å (Szkody et al. 2003; Halpern et al. 2013), 72 ± 5 Å (Pallanca et al. 2013), and 10-20 Å (Masetti et al. 2006; Pretorius 2009), respectively, when pulsations stop, and accretion, or a pulsar wind shock, produces low-level X-ray emission ($L_X \sim 10^{33}$ ergs/s).

What we take from this overview of the literature is that most quiescent NS LMXBs show H α EWs typically between 20 to 50 Å. The exception is the NS LMXBs which have swung between accretion and radio pulsar activity, which have no H α emission during their radio pulsar phase, and can have lower H α emission during their near-quiescent periods. As U24 in NGC 6397 shows no evidence of active accretion (see §4.2 on X-ray variability below), and has not been observed to be a radio pulsar despite numerous deep pulsar searches of NGC 6397, it seems unlikely that U24 falls into the latter category. We should therefore expect an H α EW between 20–50 Å, if hydrogen is present in the accreting material. Our upper limit on the H α EW of 19 Å suggests, therefore, that U24 does not possess hydrogen; and that the companion is a white dwarf. This interpretation is consistent with the weak limit that we are able to place on the $B-R$ color, which allows an object as blue as a white dwarf (much of the observed light may also come from an accretion disk).

4 X-RAY SPECTRAL FITTING

4.1 ω Cen

We begin by checking that we get similar results to Guillot et al. (2013), their Table 4 (lower part) and Fig. 6, when using the same data (though with slightly different processing and binning) and the same assumptions. We use a *wabs*nsatmos* fit to only the *XMM-Newton* pn spectrum and the (combined) 2000 *Chandra* spectrum, and fix the distance and N_H to Guillot et al.'s values ($d=4.8$ kpc, $N_H=1.82 \times 10^{21}$ cm $^{-2}$). For a fixed NS mass of $1.4 M_\odot$, we find a best-fit NS radius of 20.6 km, with 90% confidence range of 18.1–23.5 km, in good agreement with Guillot et al. (2013). We list this fit as “Guillot+13” in Table 2. (We use 90% confidence ranges throughout, unless otherwise specified.) A steppar plot calculating the permitted mass and

radius range for this fit (not shown) is in good agreement with their Fig. 6. Freeing N_H and setting the distance to our preferred value of 5.3 kpc, we find similar results; for the NS mass fixed to $1.4 M_\odot$, the best fit is $R=20.3$ km, with a range of 13.6-29.4 km.

We then check the effect of switching our ISM model to *tbabs*, using Wilms, Allen & McCray (2000) abundances and Verner et al. (1996) cross-sections, keeping our other assumptions the same. We find that for a fixed $1.4 M_\odot$ mass and 5.3 kpc distance, the best-fit NS radius is 16.3 km, with range 11.3–23.0 km. (The best-fit value of N_H remains similar, at 1.8×10^{21} cm $^{-2}$.) This is a $\sim 25\%$ change in the best-fit NS radius (or a 20% change in the radius lower limit) due to a change in the ISM model, reinforcing the critical importance of accurate modeling of the ISM. This effect seems to be due primarily to the reduction in the relative abundance of oxygen (compared to similar-Z elements) between the Anders & Ebihara (1982) and Wilms, Allen & McCray (2000) models, which leads to a shallower edge at 0.53 keV, for similar averaged interstellar absorption (see Fig. 3 for an illustration). The downward curvature of the spectrum of the neutron star at low energies is due to a combination of the declining detector response, the temperature of the NS model (i.e. the intrinsic spectral curvature), and the effect of the ISM. Thus, changing the shape of the ISM model alters how much of the observed curvature is attributed to intrinsic curvature of the spectrum, versus attributed to the effects of the ISM.

For completeness, we check the effect of using the *phabs* model with XSPEC's default abundances (Anders & Grevesse 1989) and cross-sections (Balucinska-Church & McCammon 1992), finding a best-fit radius of 24.4 (15.8 to >30) km, which is even farther from the results using *tbabs* and Wilms abundances (almost a 50% difference) than when using the *wabs* model. Details of each of these fits are listed in Table 2.

We next add in the combined MOS spectrum, and the new 2012 *Chandra* data, so we are now fitting four spectra. A *wabs*nsatmos* model fit to all the data finds a substantially smaller best-fit radius, 11.5 km (8.0–14.9 km) for a $1.4 M_\odot$ NS at 5.3 kpc. Switching to *tbabs*, with new abundances and cross-sections, shrinks the best-fit radius further, to 10.0 km (5.0–12.6 km). We note that the fitted N_H , including the new data and recent ISM modeling, is more consistent with the predicted N_H to the cluster, as suggested by Lattimer & Steiner (2014) with the rationale that it would make the NS mass and radius predictions consistent with the other datasets.

We notice a clear residual in the *XMM-Newton* pn spectrum above 1.5 keV, suggestive of a nonthermal component to the NS spectrum, as commonly observed in qLMXBs. We test the addition of a power-law component (we use the *pegpwlw* model, where the normalization is proportional to the intrinsic flux) to the spectrum, with photon index fixed to 1.0, 1.5, or 2.0 (the typical range of the spectra observed). Such a component is not detected with 90% confidence for any index, but the best fit power-law fluxes for each choice are similar, $F_X(0.5-10 \text{ keV})=6-8 \times 10^{-16}$ ergs/cm 2 /s, or a best-fit $L_X \sim 2 \times 10^{30}$ ergs/s, at 90% confidence $L_X < 9 \times 10^{30}$ ergs/s. Permitting a power-law component slightly alters the best-fit NS radius to 10.2 km (5–13.3 km), changing the best fit by less than 0.1 km if the selected pho-

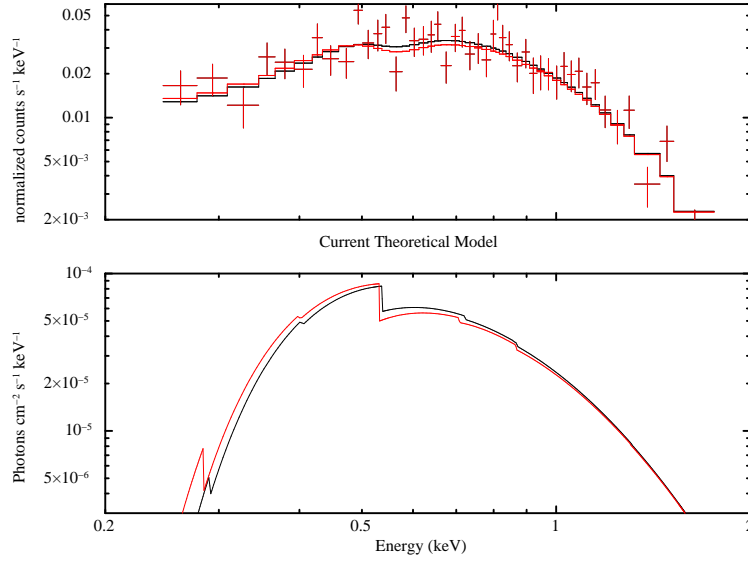


Figure 3. Illustration of the effects of using the *wabs* versus *tbabs* ISM models to fit the ω Cen qLMXB. The observed pn spectrum (crosses) and folded models (black, *tbabs* with *wilms* abundances; red, *wabs*) are plotted in the top panel, while the unfolded models are plotted in the bottom panel. The *tbabs* model plotted has a higher N_H ($1.6 \times 10^{21} \text{ cm}^{-2}$) than the *wabs* model ($1.3 \times 10^{21} \text{ cm}^{-2}$), to give similar total absorption, but the deeper 0.53 keV O edge of the *wabs* model produces a different shape to the absorption.

Table 2. X-ray spectral fits to ω Cen; comparing to Guillot+13

Fit	N_H $\times 10^{21} \text{ cm}^{-2}$	R km	M M_\odot	kT_{eff} eV	χ^2/dof
<i>wabs*nsatmos</i>					
Guillot+13, d=4.8	(1.82)	$20.6^{+2.9}_{-2.5}$	(1.4)	61^{+4}_{-3}	79.6/71
d=5.3, N_H free	$1.7^{+0.5}_{-0.4}$	$20.3^{+9.1}_{-6.7}$	(1.4)	63^{+11}_{-9}	79.3/70
<i>phabs*nsatmos</i>					
d=5.3, phabs/angr	$1.9^{+0.4}_{-0.5}$	$24.4^{+6.8}_{-8.5}$	(1.4)	60^{+10}_{-4}	80.0/70
<i>tbabs*nsatmos</i>					
d=5.3, wilm	$1.8^{+0.5}_{-0.5}$	$16.3^{+6.7}_{-5.0}$	(1.4)	68^{+12}_{-8}	79.4/70

Fits to only the *XMM-Newton*/pn and 2000 *Chandra*/ACIS data on the ω Cen qLMXB. Parameters in parentheses are fixed, others show 90% confidence errors on a single parameter. ^h-parameter reached hard limit of model. The first fit matches a similar fit in Guillot et al. (2013). See text for details of the assumptions in each fit.

ton index is altered to a different value. We fix the photon index to 1.5 below, and report the details of this fit (with mass fixed to $1.4 M_\odot$) in Table 3.

Finally, we create a *tbabs(nsatmos+pegpwlw)* fit with index=1.5 and mass free. This fit is illustrated in Figure 4, which shows all 4 spectra fit to the same model. In the line for this fit in Table 3 (line labeled “NS+PL,M free”), we provide the ranges for NS mass and radius if the other quantity is fixed at its best-fit value. In Figure 5 (left), we illustrate the full range of NS mass and radius values permitted by this fit, at 68%, 90%, and 99% confidence ranges. The allowed values are consistent, assuming typical NS masses, with the most commonly discussed NS equations of state (e.g. Lattimer & Prakash 2007). We then chose distances at the extremes of the reasonable distance range we identify above (5.13 and 5.47 kpc), and calculated probability con-

tours for mass and radius for these distances (see Figure 5, right).

We can use these data to ask whether this NS shows evidence of variability. We use the two *Chandra* spectra to measure any variation in the ω Cen NS temperature, between the years 2000 and 2012. We use the *tbabs(nsatmos+pegpwlw)* model, with d=5.3 kpc, photon index 1.5, and NS M=1.4 M_\odot . We first check whether permitting the power-law normalization to vary produces a better fit than fixing all parameters, but find that neither spectrum’s power-law component varies from zero at 90% confidence, and that an F-test indicates that untying the power-law normalization between the two spectra does not produce a better fit. We therefore tie the power-law normalizations between the two spectra, and test whether varying the NS temperature produces a superior fit. Again, it does not (the F-test gives an

Table 3. X-ray spectral fits to ω Cen, all data

Fit	N_H $\times 10^{21} \text{ cm}^{-2}$	R km	M M_\odot	kT_{eff} eV	PL flux $\text{ergs/cm}^{-2}/\text{s}$	χ^2/dof
<i>wabs*nsatmos</i>						
wabs	$1.2^{+0.3}_{-0.3}$	$11.5^{+3.4}_{-3.5}$	(1.4)	80^{+18}_{-9}	-	152.7/130
<i>tbabs*nsatmos</i>						
wilms	$1.3^{+0.3}_{-0.3}$	$10.0^{+2.6}_{-5.0^h}$	(1.4)	85^{+61}_{-9}	-	152.4/130
<i>tbabs*(nsatmos+pegpurlw)</i>						
NS+PL,M=1.4,d=5.3	$1.3^{+0.3}_{-0.3}$	$10.3^{+3.2}_{-5.3^h}$	(1.4)	83^{+55}_{-10}	$6^{+21}_{-6} \times 10^{-16}$	152.2/129
NS+PL,M free	$1.3^{+0.4}_{-0.3}$	$10.6^{+2.4}_{-1.8@}$	$0.5^{+1.6}_{-0^h@}$	74^{+44}_{-6}	$6^{+21}_{-6} \times 10^{-16}$	152.2/127

Fits to *XMM-Newton*/pn, *XMM-Newton*/MOS, 2000 and 2012 *Chandra*/ACIS data on the ω Cen qLMXB. Parameters in parentheses are fixed, others show 90% confidence errors on a single parameter. h -parameter reached hard limit of model. @-for the errors on mass and radius reported in this fit, the other parameter (e.g. radius, if mass was varied) was held fixed at its best-fit value.

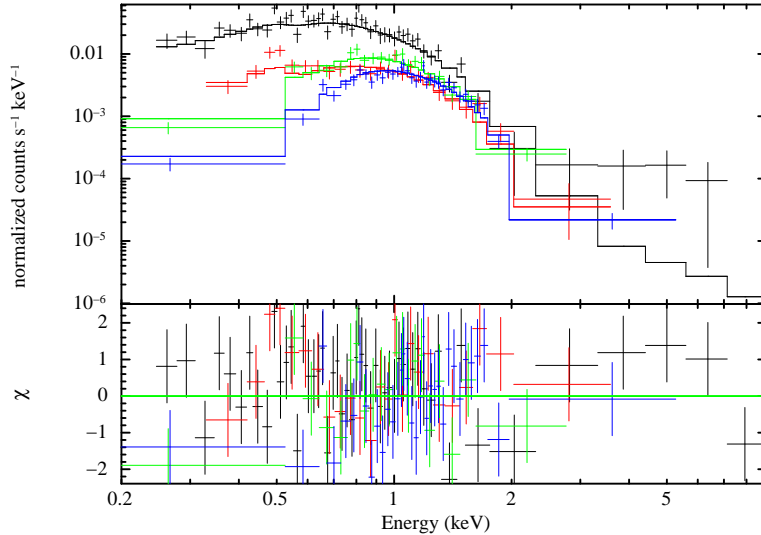


Figure 4. Fit to spectra of ω Cen qLMXB, using *tbabs(nsatmos+pegpurlw)* with index=1.5 and NS mass free. Data and model are plotted in the top panel, with residuals plotted below. Black: *XMM-Newton* pn data; red: *XMM-Newton* combined MOS data; green: *Chandra* 2000 data; blue: *Chandra* 2012 data.

F statistic of 0.657, probability of obtaining such a result by chance 0.42). We freeze all parameters at their best-fit values, except for the 2000 *Chandra* NS temperature, and measure a temperature difference of $-0.7^{+1.4}_{-1.4}\%$, at 90% confidence. Alternatively, permitting a multiplicative constant between the models used for the two spectra, and holding all other parameters the same between the models, we find the 2012 observation to show a normalization $95^{+5}_{-5}\%$ of the 2000 observation. Thus, at 90% confidence we can say that the ω Cen NS shows $<2.1\%$ temperature variation, or $<10\%$ flux variation, over 12 years.

Given the consistency of the flux over a decade, we can test how well the calibration of the *XMM-Newton* and *Chandra* instruments compare. For this purpose, we used all the data, but separated them into three groups; the *Chandra*, *XMM-Newton* pn, and *XMM-Newton* MOS spectra. We froze all parameters for the pn spectrum, and all parameters but the NS temperature for the others, and measured

the difference in NS temperature recorded by the other instruments. We found the MOS-measured temperature to be $1.6^{+1.5}_{-1.7}\%$ higher, and the *Chandra*-measured temperature to be $0.7^{+0.8}_{-0.8}\%$ lower; thus, all instruments are consistent within the 90% confidence errors. Alternatively, starting from the best fit for a fixed NS mass of $1.4 M_\odot$, we fixed all parameters at their best-fit values, then freed the MOS and *Chandra* radii. Compared to the best-fit radius (fixed for the pn) of 10.50 km, the MOS result is 10.8 ± 0.3 km, and the *Chandra* result is 10.35 ± 0.15 km, again consistent. We infer that the relative uncertainties produced by differences between detectors contribute $\lesssim 4\%$ systematic uncertainties to NS radius measurements. Of course, this does not account for possible absolute normalization uncertainties affecting all X-ray detectors, but the independent ground-based flux calibration procedures performed on the X-ray detectors (Garmire et al. 2003; Turner & et al. 2001; Strüder & et al.

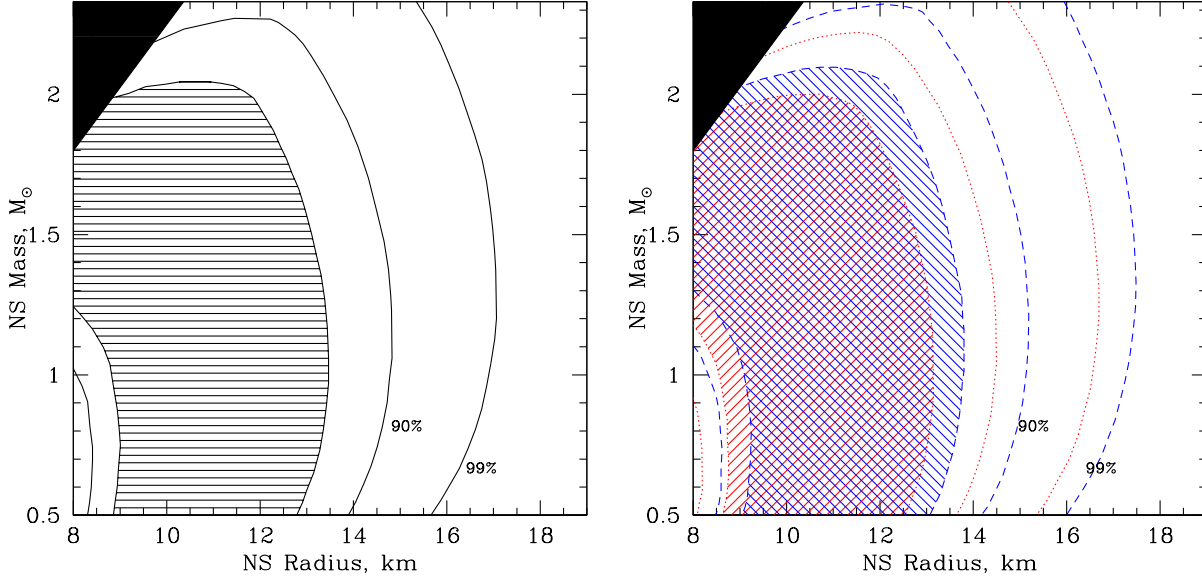


Figure 5. *Left:* Probability contours for the acceptable range of mass and radius for the ω Cen qLMXB. This fit uses *tbabs(nsatmos+pegpwlw)*, with assumed distance of 5.3 kpc and a powerlaw photon index of 1.5. The solid black region at upper left identifies the excluded region (from causality constraints). The shaded region is the 1σ region, while the outer contours indicate the 90% and 99% confidence region. *Right:* Probability contours for the ω Cen qLMXB, using the same assumptions as the left figure, except using assumed distances of 5.13 kpc (red, with $/$ shading and dotted lines) or 5.47 kpc (blue, with \backslash shading and dashed lines).

2001) indicate that such uncertainties should be of the same order at most.

The value of the fitted N_H has a very strong effect on the fitted radius of the NS. Independently constraining the N_H would thus significantly shrink the permitted region of mass and radius. Is there another reliable method to constrain the N_H ? As described above, the extinction measured towards the cluster by CMD fitting gives the best estimate of the N_H towards the cluster. However, there are two caveats to using this; a) the conversion from optical extinction ($E(B - V)$) to X-ray measured N_H is not perfectly measured or understood (see Güver & Özel 2009); and b) there may be additional N_H intrinsic to the system studied. It might be possible to eliminate caveat a) by measuring the N_H to other objects in the cluster with high precision. We attempted this using spectra from the two brightest cataclysmic variables in ω Cen (Carson, Cool & Grindlay 2000; Cool et al. 2013), extracted from the deep 2012 *Chandra* observations. However, we found that the measured N_H for each spectrum was inconsistent with, and larger than, the value predicted by the extinction to the cluster, and the N_H we measured for the qLMXB, and that the two N_H values were also inconsistent with each other. (Details of the spectral fitting of these sources will be presented elsewhere.) Thus, we conclude that we cannot effectively constrain the N_H to the ω Cen qLMXB by means other than spectral fitting.

We have shown above that the abundances used make a major difference in the interpretation of the spectra. Here we illustrate this by taking our best spectral fit to the ω Cen data, changing the abundance pattern, and investigating the resulting allowed range in mass and radius. The measured N_H may be attributed either entirely to the interstellar medium (this may vary across the face of the cluster, and

could show different abundances in different clouds), or to a mixture of interstellar N_H and N_H intrinsic to the binary. We test four fits using a single abundance pattern for the full N_H column; *wilms* from Wilms, Allen & McCray (2000) (our preferred fit), *lodd* from Lodders (2003), *aspl* from Asplund et al. (2009), and *angr* from Anders & Grevesse (1989), where the first three are modern abundance measurements (which agree fairly closely), while the fourth is currently the default abundance pattern in XSPEC. We also consider a fit where we assume a fixed interstellar N_H of $0.83 \times 10^{21} \text{ cm}^{-2}$ (matching the measured $E(B - V)$ of 0.12 reported for ω Cen by Harris 1996, using the conversion of Güver & Özel 2009), with additional N_H intrinsic to the binary. To model additional N_H intrinsic to the binary, we use the *zvfabs* model in XSPEC, with the relative abundances of iron and other metals being set to 0.03 and 0.06 respectively (to simply represent the average ω Cen abundances of [Fe/H]=-1.5 Harris 1996, and $[\alpha/\text{Fe}]=0.3$ Carney 1996).

In Figure 6, we show the 1σ confidence contours for these five abundance pattern choices. Hearteningly, there is little difference between the contours for the three modern abundance measurements. However, the Anders & Grevesse (1989) abundances make a significant difference (dramatically increasing the inferred radius, and generally making the contours wider), and we do not recommend their use. Furthermore, we see a significant effect on the contours (toward smaller radii) when assuming that any N_H above the reported cluster value has the abundances of the cluster.

4.2 NGC 6397

As above, we begin by checking that we get similar results to Guillot et al. (2013), their table 4 (lower part) and figure

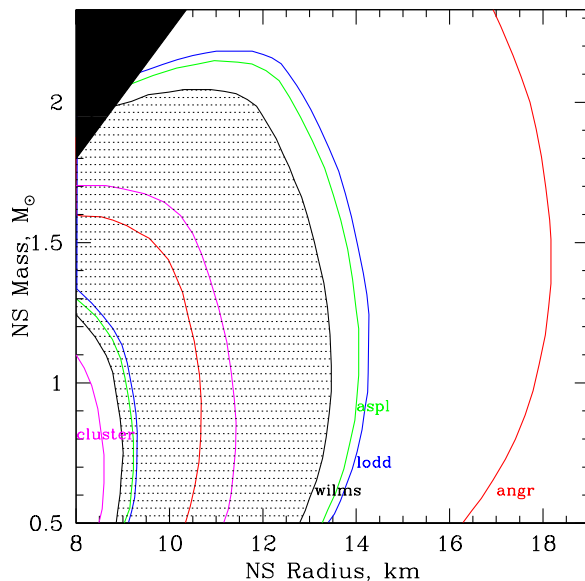


Figure 6. Five different 1σ probability contours for the acceptable range of mass and radius for the ω Cen qLMXB, depending on the abundance pattern chosen. This fit uses *tbabs(nsatmos+pow)*, with assumed distance of 5.3 kpc and a powerlaw photon index of 1.5. The solid black region at upper left identifies the excluded region (from causality constraints). The shaded (dots) region is the 1σ region for *wilms* abundances (Wilms, Allen & McCray 2000). The blue and green contours enclose the (similar) 1σ regions for the *aspl* (Asplund et al. 2009) and *lodd* (Lodders 2003) abundance choices, and the red contours enclose this region for the *angr* (Anders & Grevesse 1989) abundances. The magenta contours are for a fixed column with *wilms* abundances, plus additional N_H at the cluster abundance; see text.

6, when using the same data (though with slightly different processing and binning) and the same assumptions. Using the *wabs*nsatmos* model, assuming a 2.02 kpc distance and $N_H = 9.6 \times 10^{20} \text{ cm}^{-2}$, we find a best-fit mass, radius and temperature close to those of Guillot et al. (see Table 4). Since Guillot et al. find a best-fit mass significantly different from $1.4 M_\odot$, we report *wabs*nsatmos* fits with and without a fixed $1.4 M_\odot$ NS mass, noting that the fit using a $1.4 M_\odot$ NS is strongly disfavored. We also include a *wabs*nsatmos* fit changing the distance to our preferred 2.51 kpc value, and leaving the N_H free, which enables a reasonable fit with a $1.4 M_\odot$ NS, though the best-fit radius is uncomfortably low.

We then test the *tbabs*nsatmos* model, with Wilms, Allen & McCray (2000) abundances, and for completeness the *phabs*nsatmos* model using default (Anders & Grevesse 1989) abundances. In contrast to our ω Cen fits, we do not find dramatic discrepancies here between the different N_H models (Table 4), perhaps due to the different effective area energy dependences of the *XMM-Newton* EPIC vs. *Chandra*/ACIS detectors. If we add a power-law component, we find a significant improvement in the χ^2 (with probability 2×10^{-4} of occurring by chance, according to an F-test). The power-law photon index Γ finds a best fit at the (unphysical) value of 3.9, but is poorly constrained (range 0.5 to 4.7). Varying the index in the range (1-2) observed for other quiescent NSs (e.g. Campana et al. 1998; Cackett et al. 2010) makes little difference (e.g. the inferred radius upper limit changes by only 0.2 km); we include the fit with Γ fixed to 2.0 below as an example. Again, we see that an uncomfortably small

radius (< 9 km) is required for a $1.4 M_\odot$ NS in all physically reasonable fits using a hydrogen atmosphere.

We investigate the range of reasonable radii and masses for the last fit above, *tbabs(nsatmos+pegpurlw)*, using a 2.51 kpc distance and including a power-law, with photon index frozen to 1.5. We plot the 1σ , 90%, and 99% confidence ranges in Figure 7 (left). Clearly, the hydrogen-atmosphere fit indicates a NS smaller than 10 km, and suggests a mass below $1.4 M_\odot$. We do the same analysis for the extrema of our distance range, 2.44 and 2.58 kpc, and plot the results in Figure 7 (right).

Considering the intriguingly small radius predicted by the NSATMOS hydrogen atmosphere model, and the evidence above (§3) suggesting an ultracompact nature for the NGC 6397 qLMXB, we consider a helium atmosphere model for this object. Our helium atmosphere model, spHe, is described in Ho & Heinke (2009).⁵

We first try fitting a *tbabs*spHe* model, without the power-law component. This gives a relatively small radius ($7.5^{+2.2}_{-2.3}$ km for a $1.4 M_\odot$ NS), and a good fit. Adding a power-law component (with Γ fixed to 1.5) improves the fit (the improvement is significant at 95% confidence, according to an F-test). This fit is shown in Figure 8. The availability of the power-law increases the allowed range of radii, giving a radius range of $9.0^{+2.9}_{-4*}$ km (hitting the lower boundary of our model radius range). We find that our N_H measurement is nicely consistent with the inferred N_H from the extinction in

⁵ Now available as a local model in XSPEC, along with our carbon atmosphere models, in the NSX model package; see <https://heasarc.gsfc.nasa.gov/xanadu/xspec/models/nsx.html>

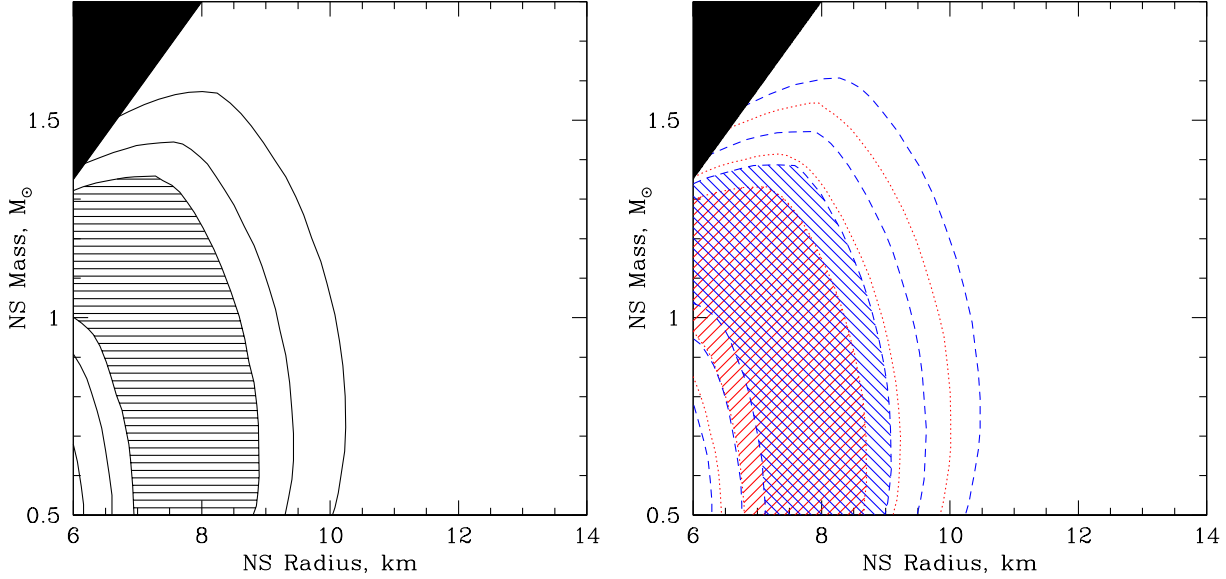


Figure 7. Probability contours for the acceptable range of mass and radius for the NGC 6397 qLMXB, using a hydrogen atmosphere. This fit uses `tbabs(nsatmos+pow)`, with assumed distance of 2.51 kpc and a powerlaw photon index of 1.5. The solid black region at upper left identifies an excluded region (from causality constraints). The shaded region is the 1σ confidence region, while the outer contours indicate the 90% and 99% confidence region. *Right:* Probability contours for the NGC 6397 qLMXB, using the same assumptions as the left figure, except using assumed distances of 2.44 kpc (red, with $/$ shading and dotted lines) or 2.58 kpc (blue, with \backslash shading and dashed lines).

Table 4. X-ray spectral fits to NGC 6397

Fit	N_H $\times 10^{21} \text{ cm}^{-2}$	R km	M M_\odot	kT_{eff} eV	PL flux $\text{ergs/cm}^{-2}/\text{s}$	χ^2/dof
<i>wabs*nsatmos</i>						
Guillot+13, d=2.02	(0.96)	$6.5^{+1.0}_{-1.5^h}$	$0.90^{+0.21}_{-0.40^h}$	78^{+10}_{-10}	-	216.2/202
Guillot+13, d=2.02	(0.96)	$6.9^{+0.2}_{-0.3}$	(1.4)	87^{+2}_{-3}	-	277.6/203
d=2.51, N_H free	$1.0^{+0.1}_{-0.1}$	$7.4^{+1.1}_{-1.4}$	(1.4)	89^{+18}_{-8}	-	219.9/202
<i>phabs*nsatmos</i>						
d=2.51, angr	$1.1^{+0.1}_{-0.1}$	$7.0^{+1.9}_{-1.2}$	(1.4)	94^{+19}_{-14}	-	220.3/202
<i>tbabs*nsatmos</i>						
d=2.51, wilm	$1.3^{+0.5}_{-0.5}$	$7.3^{+0.7}_{-1.1}$	(1.4)	89^{+13}_{-6}	-	226.9/202
<i>tbabs(nsatmos+peppwrlw)</i>						
$\Gamma=1.5$	$1.2^{+0.1}_{-0.1}$	$7.3^{+1.1}_{-1.4}$	(1.4)	88^{+19}_{-8}	$5^{+2}_{-2} \times 10^{-15}$	211.8/201
$\Gamma=2.0$	$1.2^{+0.1}_{-0.1}$	$7.4^{+1.1}_{-1.5}$	(1.4)	88^{+21}_{-8}	$6^{+2}_{-2} \times 10^{-15}$	211.4/201
$\Gamma=1.5, M$ free	$1.0^{+0.2}_{-0.2}$	$7.1^{+1.4}_{-2.1^h}$ @	$1.07^{+0.31}_{-1.07^h}$ @	82^{+43}_{-15}	$4^{+3}_{-3} \times 10^{-15}$	208.5/200
<i>tbabs(spHe)</i>						
	$1.1^{+0.2}_{-0.2}$	$7.5^{+2.2}_{-2.3}$	(1.4)	86^{+39}_{-13}	-	213.1/202
<i>tbabs(spHe+peppwrlw)</i>						
$\Gamma=1.5$	$1.2^{+0.2}_{-0.2}$	$9.0^{+2.9}_{-4^h}$	(1.4)	77^{+55}_{-11}	$3^{+3}_{-2} \times 10^{-15}$	209.1/201
$\Gamma=1.5, M$ free	$1.2^{+0.2}_{-0.2}$	$8.8^{+2.9}_{-3.3}$ @	$1.45^{+0.34}_{-0.44}$ @	78^{+32}_{-20}	$3^{+3}_{-2} \times 10^{-15}$	209.0/200

Fits to the five *Chandra/ACIS* datasets on the NGC 6397 qLMXB. Parameters in parentheses are fixed, others show 90% confidence errors on a single parameter. The first fit matches a similar fit in Guillot et al. (2013). See text for details of the assumptions in each fit. h -parameter reached hard limit of model. @-for the errors on mass and radius reported in this fit, the other parameter (e.g. radius, if mass was varied) was held fixed at its best-fit value.

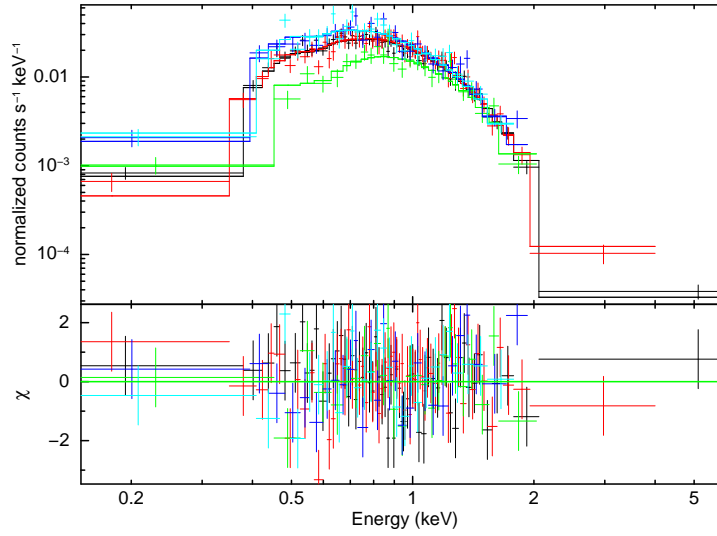


Figure 8. Fit to spectra of NGC 6397 NS, using `tbabs(spHe+pegpwr)` with `index=1.5` and NS mass free, with data and model plotted above, and residuals plotted below. Black and red: *Chandra* 2009 spectra; green: *Chandra* 2000 data; light and dark blue: *Chandra* 2002 data.

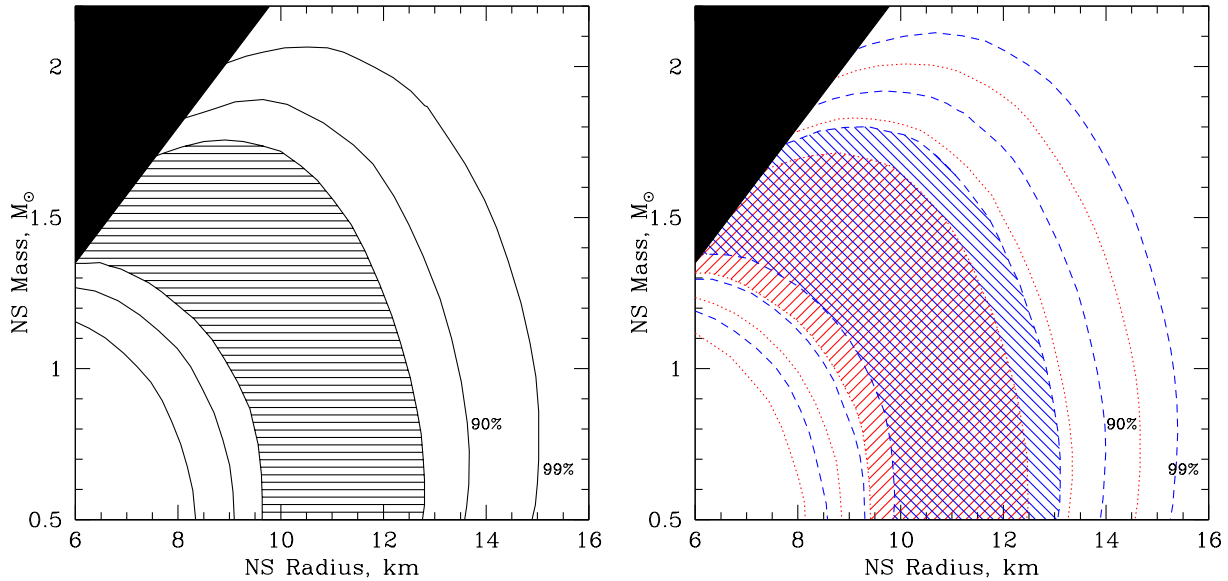


Figure 9. Probability contours for the acceptable range of mass and radius for the NGC 6397 qLMXB, using a helium atmosphere. This fit uses `tbabs(spHe+pow)`, with assumed distance of 2.51 kpc and a powerlaw photon index of 1.5. The black line at upper left identifies the excluded region (from causality constraints). The shaded region is the 1σ confidence region, while the outer contours indicate the 90% and 99% confidence region. *Right:* Probability contours for the NGC 6397 qLMXB, using the same assumptions as the left figure, except using assumed distances of 2.44 kpc (red, with ↗ shading and dotted lines) or 2.58 kpc (blue, with ↘ shading and dashed lines).

the direction of NGC 6397 (Harris 1996), as again predicted by Lattimer & Steiner (2014).

We investigate the range of reasonable radii and masses for this fit, `tbabs(spHe+pegpwlw)`, using a 2.51 kpc distance and including the power-law with photon index of 1.5. We plot the 1σ , 90%, and 99% confidence ranges in Figure 9 (left). Again, we do the same analysis for the extrema of our distance range, 2.44 and 2.58 kpc, and plot the results in Figure 9 (right). The ranges of radii and masses calculated for

the helium atmosphere model are significantly larger than those for the hydrogen atmosphere.

As for the ω Cen qLMXB above, we can test for variation in temperature or total flux among the three *Chandra* epochs. Fixing the other parameters, and the 2009 best-fit temperature, at their best-fit values, we allowed the temperature of the NS in 2000 and 2002 to vary. The NS temperature in 2000 was $-0.2^{+1.2}_{-1.2}\%$ lower than in 2009, and that in 2002 was $0.2^{+0.8}_{-0.9}\%$ higher than in 2009. Thus, we conclude that there is no evidence for variability among the ob-

servations, with temperature variations less than 1.4% (at 90% confidence) over 10 years. Guillot, Rutledge & Brown (2011) performed a similar (slightly different) analysis, and our result agrees with theirs.

Finally, we investigate the effect of different choices of abundance patterns, as for ω Cen, showing the results in Fig. 10. We see, again, that the choice of the *wilms*, *aspl*, or *lodd* abundance patterns has only a small effect on the outcome. The *anqr* (Anders & Grevesse 1989) abundance pattern again produces rather larger radii. We show two different choices of a cluster N_H column plus intrinsic absorption, with different selections of the cluster N_H value. Using the Predehl & Schmitt (1995) relation, the cluster $E(B - V)$ of 0.18 indicates $N_H = 1.0 \times 10^{21} \text{ cm}^{-2}$, while the Güver & Özel (2009) relation indicates $N_H = 1.2 \times 10^{21} \text{ cm}^{-2}$. In each case, the allowed contours are smaller than when assuming the entire column is interstellar; the larger intrinsic absorption gives significantly smaller radii, though the N_H difference is only $2 \times 10^{20} \text{ cm}^{-2}$.

5 DISCUSSION

The two qLMXBs we analyze in this paper are the objects with the most extreme suggested mass and/or radius values in the analysis of Guillot et al. (2013). In particular, the extremely low value of the inferred radius in Guillot et al. (2013)’s analysis significantly reduced their final result. Although Guillot et al. (2013) argue that their targets show consistent radii within 2σ , it is clear that the primary result of their paper—a relatively low NS radius of $9.1^{+1.3}_{-1.5} \text{ km}$ —depends on their analysis of the NGC 6397 qLMXB. Their simultaneous spectral fit omitting NGC 6397 finds a significantly larger NS radius of $10.7^{+1.7}_{-1.4} \text{ km}$, which is fully consistent with the ~ 11 – 13 km NS radius range predicted by nuclear experimental (e.g. Tsang et al. 2012) and nuclear theoretical studies (e.g. Hebeler et al. 2013).

For this reason, the consideration of a helium atmosphere for the NGC 6397 qLMXB is crucial for robust constraints on the NS radius. We have presented an optical detection of a likely candidate optical counterpart to the NGC 6397 qLMXB, and intriguing, though not conclusive, evidence in favor of a white dwarf companion, which would suggest the NS may have a helium atmosphere. Fitting the NGC 6397 qLMXB with hydrogen atmosphere models leads to an inferred radius $< 9.0 \text{ km}$ at 90% confidence, for any mass $> 1.2 M_\odot$, and within our considered distance range. Such a low NS radius would significantly disagree with the nuclear theoretical and experimental studies cited above. (Note that the lower distances inferred from dynamical distance estimates would exacerbate the discrepancy.) We conclude that a helium atmosphere is preferred for the NGC 6397 qLMXB, making it the first such qLMXB for which we have any evidence of a helium atmosphere.

We find that the choice of ISM abundance model can make a significant difference in the inferred NS radius. Furthermore, our best-fit N_H values for both the ω Cen and NGC 6397 qLMXBs are closer to the N_H inferred from the cluster optical extinction $E(B - V)$, using the Güver & Özel (2009) relation between N_H and $E(B - V)$, than the values from the fits by Guillot et al. (2013). For NGC 6397, our fitted N_H value agrees with this extinction estimate

$(1.2 \pm 0.2 \times 10^{21} \text{ cm}^{-2}, \text{ vs. } 1.2 \times 10^{21} \text{ cm}^{-2})$. However, for ω Cen, our fitted N_H value remains well above the cluster extinction estimate $(1.3 \pm 0.3 \times 10^{21} \text{ cm}^{-2}, \text{ vs. } 0.83 \times 10^{21} \text{ cm}^{-2})$, which does not account for small-scale variations. We agree with Guillot et al. (2013) that spectral fitting is the only reliable way to determine the N_H to a particular X-ray source. Considering the strong dependence of the inferred NS radius on details of the ISM abundance model, it is clear that the best targets for further constraints on the NS radius should have low N_H values.

We find no evidence of variability among multiple observations of the ω Cen and NGC 6397 qLMXBs over decade timescales, constraining their temperature fluctuations to $< 2.1\%$ and $< 1.4\%$ respectively. Combined with the strong constraints on variation of the M28 qLMXB (Servillat et al. 2012) and X7 in 47 Tuc (Heinke et al. 2006), we now have four qLMXBs that show little or no power-law component and with strong constraints on temperature variability over multi-year timescales. This is evidence in favor of the suggestion (Heinke et al. 2003) that the strength of the power-law component indicates the strength of any continuing accretion, and thus that the thermal emission from qLMXBs showing no power-law component is powered entirely by deep crustal heating (Brown, Bildsten & Rutledge 1998).

We can ask the question of what the inferred orbital period of the NGC 6397 qLMXB might be, if it is ultracompact and its thermal emission is powered by deep crustal heating. Using the “standard cooling” curve relating the mass transfer rate and bolometric NS luminosity of Yakovlev & Pethick (2004), and our calculated bolometric quiescent L of $2.0 \times 10^{32} \text{ ergs/s}$, we estimate a mass transfer rate of $2.5 \times 10^{-12} M_\odot/\text{year}$. Using the ultracompact X-ray binary evolution track of Deloye & Bildsten (2003), we can thus predict an orbital period of 50 minutes for this system. If the NS experiences enhanced neutrino cooling, then the mass transfer rate would be higher, and the orbital period could be lower, down to 21 minutes (the minimum for transient helium-accreting ultracompact X-ray binaries; Lasota, Dubus & Kruk 2008).

Our constraints on the mass and radius of the ω Cen and NGC 6397 qLMXBs are not extremely constraining. However, our results remove the evidence pointing towards a small NS radius advanced by Guillot et al. (2013). Latimer & Steiner (2014) argued for different choices of N_H and helium atmospheres for some of the five sources studied by Guillot et al. (2013). Using analytical prescriptions to alter the inferred NS mass and radius ranges of Guillot et al. to match their choices, and including information about the behavior of neutron matter at low densities, and the NS maximum mass, they then calculated a larger inferred NS radius. Our analysis can be taken as overall support for their arguments, as we provide explicit observational support for different choices of N_H and for a helium atmosphere model, although the details are significantly different.

Acknowledgements

We thank G. R. Sivakoff for helpful comments. COH is supported by an NSERC Discovery Grant and an Alberta Ingenuity New Faculty Award. DH and AMC are supported by *Chandra* Award Numbers GO2-13057A and GO2-13057B issued by the CXO, which is operated by the Smithsonian Astrophysical Observatory for and on behalf of NASA under contract NAS8-03060. Based in part on observations with

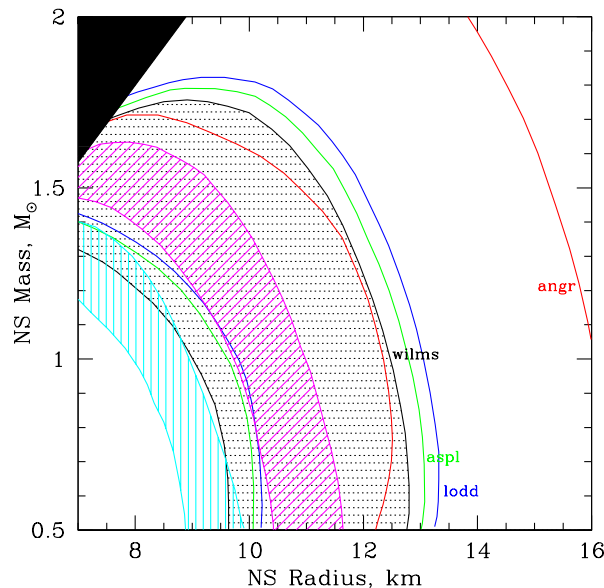


Figure 10. Six different 1σ probability contours for the acceptable range of mass and radius for the NGC 6397 qLMXB, depending on the abundance pattern chosen. This fit uses *tbabs*(*spHe*+*pegwrlw*), with an assumed distance of 2.51 kpc and a powerlaw photon index of 1.5. The region shaded with black dots is the 1σ region for *wilms* abundances (Wilms, Allen & McCray 2000), as in Fig. 8. The blue and green contours enclose the (similar) 1σ regions for the *aspl* (Asplund et al. 2009) and *lodd* (Lodders 2003) abundance choices, and the red contours enclose this region for the *angr* (Anders & Grevesse 1989) abundances. The magenta contours (shaded at 45° angle) are for a fixed column of $1.2 \times 10^{21} \text{ cm}^{-2}$ with *wilms* abundances, plus additional N_H at the cluster abundance; the cyan contours (shaded vertically) are the same, except the fixed column is at $1.0 \times 10^{21} \text{ cm}^{-2}$.

the NASA/ESA Hubble Space Telescope, obtained at the Space Telescope Science Institute, which is operated by the Association of Universities for Research in Astronomy, Inc., under NASA contract NAS5-26555. These observations are associated with proposal GO-10257. Support for program GO-10257 was provided by NASA through a grant from the Space Telescope Science Institute, which is operated by the Association of Universities for Research in Astronomy, Inc., under NASA contract NAS 5-26555. A portion of these results were based on observations obtained with *XMM-Newton*, an ESA science mission with instruments and contributions directly funded by ESA Member States and NASA. This research made use of data obtained through observations made by NASA’s *Chandra X-ray Observatory*, data obtained from the *Chandra* Data Archive, and data obtained from the High Energy Astrophysics Science Archive Research Center (HEASARC), provided by NASA’s Goddard Space Flight Center. This research has made use of the NASA Astrophysics Data System (ADS), the electronic archive arXiv.org maintained by Cornell University Library, and software provided by the *Chandra* X-ray Center (CXC) in the application package CIAO.

REFERENCES

- Alcock C., Illarionov A., 1980, *ApJ*, 235, 534
 AlGendy M., Morsink S. M., 2014, *ArXiv e-prints*
 Altamirano D., Patruno A., Markwardt C. B., et al., 2010, *ApJL*, 712, L58
 Anders E., Ebihara M., 1982, *GeCoA*, 46, 2363
 Anders E., Grevesse N., 1989, *Geochimica et Cosmochimica Acta*, 53, 197
 Anderson J. et al., 2008, *AJ*, 135, 2055
 Archibald A. M. et al., 2009, *Science*, 324, 1411
 Asplund M., Grevesse N., Sauval A. J., Scott P., 2009, *ARAAS*, 47, 481
 Bahramian A., Heinke C. O., Sivakoff G. R., Gladstone J. C., 2013, *ApJ*, 766, 136
 Balucinska-Church M., McCammon D., 1992, *ApJ*, 400, 699
 Baraffe I., Chabrier G., Allard F., Hauschildt P. H., 1997, *A&A*, 327, 1054
 Bassa C. G., Jonker P. G., Steeghs D., Torres M. A. P., 2009, *MNRAS*, 399, 2055
 Bassa C. G. et al., 2014, *MNRAS*, 441, 1825
 Beccari G., De Marchi G., Panagia N., Pasquini L., 2014, *MNRAS*, 437, 2621
 Bildsten L., Salpeter E. E., Wasserman I., 1993, *ApJ*, 408, 615
 Bogdanov S., van den Berg M., Heinke C. O., Cohn H. N., Lugger P. M., Grindlay J. E., 2010, *ApJ*, 709, 241
 Bono G. et al., 2008, *ApJL*, 686, L87
 Brown E. F., Bildsten L., Chang P., 2002, *ApJ*, 574, 920
 Brown E. F., Bildsten L., Rutledge R. E., 1998, *ApJL*, 504, L95
 Cackett E. M., Brown E. F., Miller J. M., Wijnands R., 2010, *ApJ*, 720, 1325
 Campana S., Colpi M., Mereghetti S., Stella L., Tavani M., 1998, *A&A Rev.*, 8, 279
 Campana S. et al., 2004, *ApJL*, 614, L49
 Caputo F., degl’Innocenti S., Marconi M., 2002, in *Astronomical Society of the Pacific Conference Series*, Vol. 265,

- Omega Centauri, A Unique Window into Astrophysics, van Leeuwen F., Hughes J. D., Piotto G., eds., p. 185
- Carney B. W., 1996, *PASP*, 108, 900
- Carson J. E., Cool A. M., Grindlay J. E., 2000, *ApJ*, 532, 461
- Casares J., Dubus G., Shahbaz T., Zurita C., Charles P. A., 2002, *MNRAS*, 329, 29
- Catuneanu A., Heinke C. O., Sivakoff G. R., Ho W. C. G., Servillat M., 2013, *ApJ*, 764, 145
- Chevalier C., Ilovaisky S. A., Leisy P., Patat F., 1999, *A&A*, 347, L51
- Cohn H. N. et al., 2010, *ApJ*, 722, 20
- Cool A. M., Haggard D., Arias T., Brochmann M., Dorfman J., Gafford A., White V., Anderson J., 2013, *ApJ*, 763, 126
- Cumming A., 2003, *ApJ*, 595, 1077
- D’Avanzo P., Campana S., Casares J., Israel G. L., Covino S., Charles P. A., Stella L., 2005, *A&A*, 444, 905
- De Marchi G., Panagia N., Romaniello M., 2010, *ApJ*, 715, 1
- Del Principe M. et al., 2006, *ApJ*, 652, 362
- Deloye C. J., Bildsten L., 2003, *ApJ*, 598, 1217
- Deloye C. J., Heinke C. O., Taam R. E., Jonker P. G., 2008, *MNRAS*, 391, 1619
- Deufel B., Dullemond C. P., Spruit H. C., 2001, *A&A*, 377, 955
- Dickey J. M., Lockman F. J., 1990, *ARAA*, 28, 215
- Fender R. P., Russell D. M., Knigge C., Soria R., Hynes R. I., Goad M., 2009, *MNRAS*, 393, 1608
- Fruchter A. S., Hook R. N., 2002, *PASP*, 114, 144
- Fruscione A. et al., 2006, in *Society of Photo-Optical Instrumentation Engineers (SPIE) Conference Series*, Vol. 6270, *Society of Photo-Optical Instrumentation Engineers (SPIE) Conference Series*
- Galloway D. K., Lampe N., 2012, *ApJ*, 747, 75
- Garcia M. R., Callanan P. J., McCarthy J., Eriksen K., Hjellming R. M., 1999, *ApJ*, 518, 422
- Garmire G. P., Bautz M. W., Ford P. G., Nousek J. A., Ricker, Jr. G. R., 2003, in *Society of Photo-Optical Instrumentation Engineers (SPIE) Conference Series*, Vol. 4851, *X-Ray and Gamma-Ray Telescopes and Instruments for Astronomy*, Truemper J. E., Tananbaum H. D., eds., pp. 28–44
- Gendre B., Barret D., Webb N. A., 2003, *A&A*, 400, 521
- Gratton R. G., Bragaglia A., Carretta E., et al., 2003, *A&A*, 408, 529
- Grindlay J. E., Heinke C. O., Edmonds P. D., Murray S. S., Cool A. M., 2001, *ApJL*, 563, L53
- Guillot S., Rutledge R. E., Bildsten L., Brown E. F., Pavlov G. G., Zavlin V. E., 2009, *MNRAS*, 392, 665
- Guillot S., Rutledge R. E., Brown E. F., 2011, *ApJ*, 732, 88
- Guillot S., Servillat M., Webb N. A., Rutledge R. E., 2013, *ApJ*, 772, 7
- Güver T., Özel F., 2009, *MNRAS*, 400, 2050
- Haakonsen C. B., Turner M. L., Tacik N. A., Rutledge R. E., 2012, *ApJ*, 749, 52
- Haggard D., Cool A. M., Anderson J., Edmonds P. D., Callanan P. J., Heinke C. O., Grindlay J. E., Bailyn C. D., 2004, *ApJ*, 613, 512
- Haggard D., Cool A. M., Davies M. B., 2009, *ApJ*, 697, 224
- Haggard D., Cool A. M., Heinke C. O., van der Marel R., Cohn H. N., Lugger P. M., Anderson J., 2013, *ApJL*, 773, L31
- Halpern J. P., Gaidos E., Sheffield A., Price-Whelan A. M., Bogdanov S., 2013, *The Astronomer’s Telegram*, 5514, 1
- Hameury J. M., Heyvaerts J., Bonazzola S., 1983, *A&A*, 121, 259
- Hansen B. M. S. et al., 2007, *ApJ*, 671, 380
- Hansen B. M. S. et al., 2013, *Nature*, 500, 51
- Harris W. E., 1996, *AJ*, 112, 1487
- Hartman J. M. et al., 2008, *ApJ*, 675, 1468
- Hebel K., Lattimer J. M., Pethick C. J., Schwenk A., 2013, *ApJ*, 773, 11
- Heinke C. O., Grindlay J. E., Lugger P. M., Cohn H. N., Edmonds P. D., Lloyd D. A., Cool A. M., 2003, *ApJ*, 598, 501
- Heinke C. O., Rybicki G. B., Narayan R., Grindlay J. E., 2006, *ApJ*, 644, 1090
- Heyl J. S. et al., 2012, *ApJ*, 761, 51
- Ho W. C. G., Heinke C. O., 2009, *Nature*, 462, 71
- in’t Zand J. J. M., Cumming A., van der Sluys M. V., Verbunt F., Pols O. R., 2005, *A&A*, 441, 675
- Krauss L. M., Chaboyer B., 2003, *Science*, 299, 65
- Lasota J.-P., Dubus G., Kruk K., 2008, *A&A*, 486, 523
- Lattimer J. M., Prakash M., 2007, *Phys. Rep.*, 442, 109
- Lattimer J. M., Steiner A. W., 2014, *ApJ*, 784, 123
- Lloyd D. A., 2003, *astro-ph/0303561*
- Lodders K., 2003, *ApJ*, 591, 1220
- Masetti N., Orlandini M., Palazzi E., Amati L., Frontera F., 2006, *A&A*, 453, 295
- McDonald I., van Loon J. T., Decin L., Boyer M. L., Dupree A. K., Evans A., Gehr R. D., Woodward C. E., 2009, *MNRAS*, 394, 831
- Morrison R., McCammon D., 1983, *ApJ*, 270, 119
- Nevalainen J., David L., Guainazzi M., 2010, *A&A*, 523, A22
- Özel F., Baym G., Güver T., 2010, *Phys. Rev. D*, 82, 101301
- Pallanca C., Dalessandro E., Ferraro F. R., Lanzoni B., Beccari G., 2013, *ApJ*, 773, 122
- Papitto A. et al., 2013, *Nature*, 501, 517
- Platais I., Wyse R. F. G., Hebb L., Lee Y.-W., Rey S.-C., 2003, *ApJL*, 591, L127
- Predehl P., Schmitt J. H. M. M., 1995, *A&A*, 293, 889
- Pretorius M. L., 2009, *MNRAS*, 395, 386
- Rajagopal M., Romani R. W., 1996, *ApJ*, 461, 327
- Rees, Jr. R. F., 1996, in *Astronomical Society of the Pacific Conference Series*, Vol. 92, *Formation of the Galactic Halo...Inside and Out*, Morrison H. L., Sarajedini A., eds., p. 289
- Rees, Jr. R. F., 1997, in *Astronomical Society of the Pacific Conference Series*, Vol. 127, *Proper Motions and Galactic Astronomy*, Humphreys R. M., ed., p. 109
- Richer H. B. et al., 2008, *AJ*, 135, 2141
- Richer H. B., Heyl J., Anderson J., Kalirai J. S., Shara M. M., Dotter A., Fahlman G. G., Rich R. M., 2013, *ApJL*, 771, L15
- Romani R. W., 1987, *ApJ*, 313, 718
- Rutledge R. E., Bildsten L., Brown E. F., Pavlov G. G., Zavlin V. E., 2002a, *ApJ*, 578, 405
- Rutledge R. E., Bildsten L., Brown E. F., Pavlov G. G., Zavlin V. E., 2002b, *ApJ*, 577, 346
- Servillat M., Heinke C. O., Ho W. C. G., Grindlay J. E.,

- Hong J., van den Berg M., Bogdanov S., 2012, MNRAS, 423, 1556
- Shahbaz T., Smale A. P., Naylor T., Charles P. A., van Paradijs J., Hassall B. J. M., Callanan P., 1996, MNRAS, 282, 1437
- Steiner A. W., Lattimer J. M., Brown E. F., 2010, ApJ, 722, 33
- Strickler R. R., Cool A. M., Anderson J., Cohn H. N., Lugger P. M., Serenelli A. M., 2009, ApJ, 699, 40
- Strüder L., et al., 2001, A&A, 365, L18
- Szkody P. et al., 2003, AJ, 126, 1499
- Thompson I. B., Kaluzny J., Pych W., Burley G., Krzeminski W., Paczyński B., Persson S. E., Preston G. W., 2001, AJ, 121, 3089
- Thorstensen J. R., Armstrong E., 2005, AJ, 130, 759
- Torres M. A. P., Casares J., Martínez-Pais I. G., Charles P. A., 2002, MNRAS, 334, 233
- Tsang M. B. et al., 2012, Phys. Rev. C, 86, 015803
- Tsujimoto M. et al., 2011, A&A, 525, A25
- Turner M. J. L., et al., 2001, A&A, 365, L27
- van de Ven G., van den Bosch R. C. E., Verolme E. K., de Zeeuw P. T., 2006, A&A, 445, 513
- Verner D. A., Ferland G. J., Korista K. T., Yakovlev D. G., 1996, ApJ, 465, 487
- Webb N. A., Barret D., 2007, ApJ, 671, 727
- Wilms J., Allen A., McCray R., 2000, ApJ, 542, 914
- Woodley K. A. et al., 2012, AJ, 143, 50
- Worpel H., Galloway D. K., Price D. J., 2013, ApJ, 772, 94
- Yakovlev D. G., Pethick C. J., 2004, ARAA, 42, 169
- Zamfir M., Cumming A., Galloway D. K., 2012, ApJ, 749, 69
- Zavlin V. E., Pavlov G. G., Shibano Y. A., 1996, A&A, 315, 141
- Zurek D. R., Knigge C., Maccarone T. J., Dieball A., Long K. S., 2009, ApJ, 699, 1113